Journal of Hazardous Materials 170 (2009) 479–486

Contents lists available at ScienceDirect

Journal of Hazardous Materials

journal homepage: www.elsevier.com/locate/jhazmat

# Photo-reductive decolorization of an azo dye by natural sphalerite: Case study of a new type of visible light-sensitized photocatalyst

Yan Li[a], Anhuai Lu[a,*], Song Jin[b,c], Changqiu Wang[a]

[a] The Key Laboratory of Orogenic Belts and Crustal Evolution, School of Earth and Space Sciences, Peking University, Yiheyuan Road 5#, Haidian District, Beijing 100871, China
[b] Department of Civil and Architectural Engineering, University of Wyoming, Laramie, WY 82071, USA
[c] MWH Americas, 3665 JFK Parkway, Suite 206, Fort Collins, CO 80525, USA

ARTICLE INFO

*Article history:*
Received 11 December 2008
Received in revised form 19 April 2009
Accepted 20 April 2009
Available online 3 May 2009

*Keywords:*
Azo dye
Wastewater
Photocatalysis
Photo-reduction
Sphalerite

ABSTRACT

Natural sphalerite, which represents a new class of mineral-based catalyst, was characterized and investigated for photo-reduction of an azo dye methyl orange (MO) under visible light. After 2 h of visible light irradiation, a complete decolorization of the MO solution was achieved. The degradation rate was related to the pH conditions. Spectra from FT-IR analysis indicate an initial adsorption of MO to sphalerite via its sulfonate group. Further reduction of the adsorbed MO by sphalerite under light irradiation led to the destruction of the azo structure, as indicated by the results from UV–vis, FT-IR and ESI-MS analyses. The visible light-induced photocatalytic reductive activity of natural sphalerite was mainly attributed to the distribution of foreign metal atoms in its crystal lattice, which reduces the intrinsic bandgap of sphalerite and also broadens its spectra responding range. In addition, the high conduction band potential of natural sphalerite may also enhance the photo-reduction of MO.



## 1. Introduction

Azo dye is one of the major environmental contaminants produced from textile and other industrial processes [1]. Discharge of these dye-containing wastewaters in the environment exposes great threats to human and ecological health due to the toxicity and potential carcinogenicity of the azo dye compounds [2]. Extensive studies have been conducted to address wastewaters containing azo dyes. Treatments using physical methods (e.g., adsorption) [3]; chemical methods (e.g., oxidation and reduction) [4,5]; biological methods [6,7]; membranes [8]; and electrochemical processes [8] have been well studied and applied to address dye contaminants during the past decades. These methods are usually site specific; and sometimes elevated costs and potential generation of secondary contaminants may hinder their use. Recently, alternative techniques such as photocatalysis by semiconductor minerals for treating dye compounds have been studied. For example, photocatalysis was used as a pre-treatment for biological treatment of dye-containing wastewater, due to the recalcitrance of dye compounds to microbial degradation [9].

Among those synthetic semiconductors that have been studied for the decolorization of azo dyes, special attention has been paid to sphalerite because its large negative conduction band potential (−1.4 V vs. SCE) [10] is thermodynamically suitable for photo-reduction of azo dyes. By photo-reduction, the azo bond –N=N– in the chromophore of azo dyes could be broken to give aromatic amines that are more amenable to the follow-up biodegradation [11]. The destruction of azo bond –N=N– in the chromophore of azo dyes also leads to the decolorization of the dye-containing wastewater.

Nonetheless, the low sensitivity to solar light and high cost in synthesizing these semiconductors tend to limit their applications in photocatalysis. Development of environment friendly, cost-effective and visible light responsive photocatalyst is in high demand. Compared with synthetic sphalerite, naturally occurring sphalerite is of lower cost and readily accessible. Furthermore, our previous studies demonstrated that natural sphalerite is well responsive to visible light [12]. Unlike synthetic sphalerite, natural sphalerite consists of various impurity elements and complicated crystal lattice defects, which impose new variables to the photocatalytic processes. A study of photocatalysis by natural sphalerite is therefore necessary for evaluating its practical applications such as decolorization of azo dye in wastewaters.

In this work, the photo-degradation mechanisms of natural sphalerite were investigated by using methyl orange (MO) as a model dye compound, which is a typical organic azo dye widely used in the textile industry [13]. This study also included characterizations of natural sphalerite as the photocatalyst, analysis of its UV–vis diffuse reflectance spectra and identification of the degrada-

* Corresponding author. Tel.: +86 10 62753555; fax: +86 10 1062753555.
*E-mail address:* ahlu@pku.edu.cn (A. Lu).

0304-3894/$ – see front matter © 2009 Elsevier B.V. All rights reserved.
doi:10.1016/j.jhazmat.2009.04.071

tive intermediates and final products during photo-reduction of MO by natural sphalerite.

## 2. Experimental

### 2.1. Materials

Natural sphalerite ore from a carbonate-hosted lead-zinc deposit in hydrothermal systems of Yunnan (China) was used as the photocatalyst in this study. The sample showed a grey color and a compact-grain structure in hydrothermal veins. Associated minerals included quartz and calcite. After gravitational separation and flotation, the concentrated ore of sphalerite was ground into powder and then sieved into grains in size of 340-mesh, corresponding to the particle size below 45 μm.

The azo dye used in this work was MO, which is stable to visible and near UV light [10] but can be potentially photo-reduced in the presence of semiconductor [5]. Ascorbic acid (AA) was used as a sacrificial hole scavenger. All chemicals and reagents used in this work were A.R. grade and purchased from the Beijing Chemical Reagents Company (Beijing, China). All experiments were carried out by using deionized water.

### 2.2. Catalyst characterization

X-ray diffraction (XRD) patterns were recorded using a Japan DMAX-2400 with a secondary graphite crystal monochromator at 40 kV/100 mA. The X-ray source was Cu $K\alpha_1$ ($\lambda$ = 1.5406 Å). The lattice parameters were calculated by Unit Cell software. The chemical compositions of natural sphalerite were determined by using a JXA 8100 electron microprobe (EMPA) with a 15 kV acceleration voltage and 10 nA beam current. The standards employed were natural minerals from the Society of the Plastics Industry, Inc. (SPI) and pure elemental cadmium. The compositions of 10 randomly selected particles were analyzed by EMPA. Room-temperature Raman-scattering measurements were carried out in the spectral range of 100–800 $cm^{-1}$ by using a Renishaw RM1000 micro-Raman system. The He–Cd laser beam was utilized to excite the sample through the 50× objective of a confocal microscope. The back-scattered radiation was collected and analyzed with a thermo-electrically cooled CCD array detector. Nitrogen adsorption–desorption measurements were performed at 77 K on a Micromeritics ASAP 2000 system to obtain the Brunauer–Emmett–Teller (BET) surface area. The surface morphology of natural sphalerite was examined by using a Tecnai 20 scanning electron microscope (SEM). The zeta-potential of the catalyst was measured for suspensions containing 0.5 g/L of sphalerite in 0.1 M NaCl electrolyte solution with model Zetasizer 2000 micro-electrophoresis apparatus (Malvern). Dissolved oxygen was not purged from the suspensions. The pH was adjusted by adding HCl or NaOH. The point of zero charge (PZC) of the catalyst was obtained by measuring the zeta-potential at room temperature (25 °C). Diffuse reflectance spectra (DRS) were scanned using a Lambda 950 UV–vis spectrophotometer with an integrating sphere from 350 to 780 nm. The slit width was 2.00 nm.

### 2.3. Apparatus

The experimental apparatus used for carrying out the photocatalytic reactions consists of a light source, two UV cutoff filters and two reactors, as described by Li et al. [12]. A 500 W high-pressure tungsten halogen lamp (Philips) with light emission wavelength >300 nm was used as the visible light source. The lamp was placed 16 cm away from the reactor, and a 380 nm cutoff filter (Spectronics Corporation, USA) was used to block the UV light. The average light intensity reaching the reactor was approximately 347 $mW/cm^2$, measured by a FZ-A radiometer (Photoelectric Instrument Factory of Beijing Normal University, China). Cooling water was cycled through a cylindrical jacket around the lamp to eliminate heat influence on the system.

### 2.4. Procedure

Adsorption experiments were conducted in the dark by mixing sphalerite powder (1.0 g/L) with MO ($3 \times 10^{-5}$ M) and AA solution (0.01 M) at pH 3.3 (unadjusted). Preliminary experiments performed for 6 h under constant stirring demonstrated that an equilibrium was reached at 2 h. Therefore measurements in this study on the centrifuged sphalerite powder started after 2 h during the adsorption experiments in the dark. Photocatalytic experiments were conducted by adding 0.1 g of sphalerite powder into a reactor containing $3 \times 10^{-5}$ M MO and 0.01 M AA solution. The volume of the aqueous solution was 100 mL. The experiments were carried out at room temperature (25 °C) with the solution under constant stirring. Before illumination, the suspension was stirred in the dark for 2 h to reach the adsorption–desorption equilibrium. Blank experiment without any catalysts was conducted simultaneously. Except for experiments on pH effects, the pH reading of all reaction systems was 3.3 without adjustment. In experiments on pH effects, the pH adjustments were conducted at the beginning of the experiments by varying the ratio of ascorbic acid to sodium ascorbate. The buffering capacity of the ascorbic–ascorbate mixtures maintained the pH at the correspondingly designed values throughout the experimental periods [14].

### 2.5. Analyses

Before analysis, each aqueous solution was centrifuged to collect the photocatalyst. The supernatant solution was measured for the adsorption spectra of MO to monitor the photo-reduction. The concentration of MO was analyzed by a HP 8453 UV spectrophotometer. The adsorption of MO on natural sphalerite and the aqueous solution after photocatalytic reaction were characterized by FT-IR spectrometry (Nicolet 910) at a resolution of 4 $cm^{-1}$ with KBr beam-splitter. The analyzed solid samples were mixed with KBr powder and pressed into a pellet for FT-IR measurement. The aqueous solution was dropped on the glass slide, and dehydrated under 40 °C for 0.5 h before FT-IR analysis. Background was corrected by using a reference KBr pellet. The formation of intermediates and products were detected by FT-IR spectrometry and ESI-MS (APEXII).

## 3. Results and discussion

### 3.1. Characteristics of natural sphalerite

The XRD pattern of natural sphalerite was shown in Fig. 1. As compared with JCPDS 05-0566 data files, the sharp peaks at $2\theta$ of 28.5°, 47.5° and 56.4° correspond to (1 1 1), (2 2 0) and (3 1 1), respectively, indicating that the sample belonged to cubic sphalerite phase. The calculated lattice parameter is $a_0$ = 5.4114 Å, larger than the standard value (JCPDS 05-0566; $a_0$ = 5.4060 Å).

The element analyses of 10 measurement spots were investigated by EMPA to show the heterogeneity of the natural sphalerite (Table 1). Stoichiometric sphalerite is cubically packed in sulfur with half the tetrahedral sites occupied by zinc. However, natural sphalerite always contains minor and trace elements embedded into the crystal structure, presenting a variable stoichiometry. The EMPA data shows that Fe comprises the vast majority of the impurities of natural sphalerite. The Fe-rich sphalerite contains variable amounts of Fe, which is specific due to the complicated forming process in nature. The typical chemical formula of the natural sphalerite sample, as derived from the data (Table 1) is $(Zn_{0.936}Fe_{0.045}Cd_{0.001})_{0.982}S$.

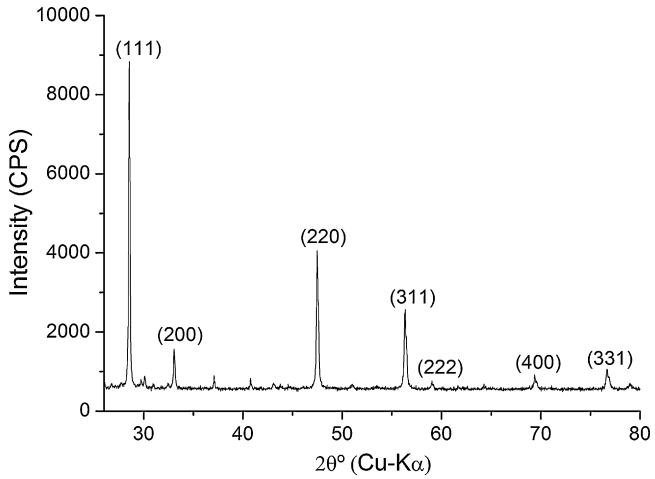


**Fig. 1.** XRD pattern of natural sphalerite (Cu $K\alpha_1$: $\lambda$ = 1.5406 Å, accelerating voltage: 40 kV, emission current: 100 mA, step-scan rate: 0.5° $min^{-1}$, step length: 0.02°).

**Table 1**
Chemical compositions of natural sphalerite particles (wt%).

| Spots | S | Zn | Fe | Cd | Mn | Ge | Se | Ga | Cu | Total |
|---|---|---|---|---|---|---|---|---|---|---|
| 1 | 33.30 | 62.27 | 3.84 | 0.12 | 0.03 | 0.01 | 0.05 | 0.08 | 0.00 | 99.69 |
| 2 | 32.73 | 62.16 | 4.21 | 0.17 | 0.01 | 0.00 | 0.02 | 0.00 | 0.00 | 99.30 |
| 3 | 33.76 | 64.72 | 0.27 | 0.23 | 0.01 | 0.05 | 0.06 | 0.03 | 0.00 | 99.14 |
| 4 | 33.18 | 63.66 | 2.57 | 0.17 | 0.00 | 0.01 | 0.20 | 0.00 | 0.03 | 99.83 |
| 5 | 33.24 | 62.64 | 3.33 | 0.13 | 0.01 | 0.00 | 0.00 | 0.01 | 0.00 | 99.40 |
| 6 | 33.11 | 64.17 | 2.06 | 0.10 | 0.02 | 0.04 | 0.00 | 0.09 | 0.00 | 99.59 |
| 7 | 32.73 | 62.87 | 3.27 | 0.19 | 0.03 | 0.05 | 0.00 | 0.00 | 0.02 | 99.17 |
| 8 | 33.50 | 63.82 | 2.61 | 0.17 | 0.01 | 0.00 | 0.00 | 0.00 | 0.10 | 100.23 |
| 9 | 34.00 | 62.83 | 3.04 | 0.11 | 0.06 | 0.10 | 0.01 | 0.03 | 0.02 | 100.22 |
| 10 | 32.88 | 65.12 | 1.01 | 0.15 | 0.01 | 0.06 | 0.07 | 0.00 | 0.02 | 99.33 |

The Raman spectrum for natural and pure sphalerite was shown in Fig. 2. The spectrum indicates the fundamental, combination, and two phonon bands, based on parameters reported by Krauzman [15]. Results demonstrate a pure sulfide phase of cubic sphalerite. The Raman spectra of pure sphalerite revealed the longitudinal-optic (LO) (mode at 349 $cm^{-1}$ [16], which was attributed to the main Zn–S band. In the case of natural sphalerite, a shift of the major Zn–S band to a lower frequency (347 $cm^{-1}$) was observed. It could be explained by the differences in the ordering of the atoms within

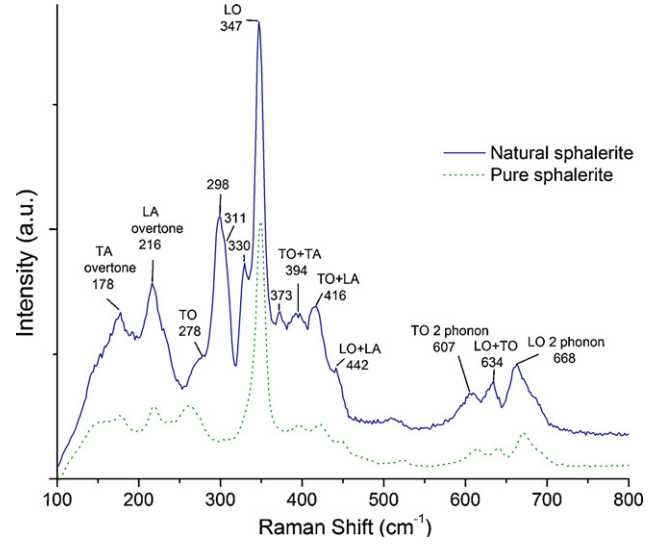


**Fig. 2.** Raman spectra of natural and synthetic pure sphalerite.

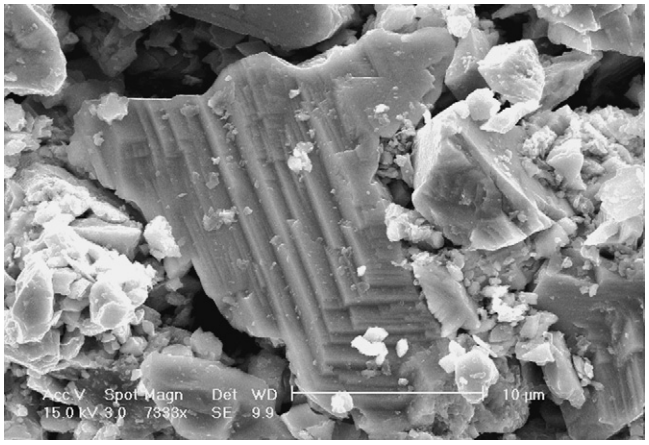


**Fig. 3.** SEM morphology of natural sphalerite.

the crystal structure [17], which indicated the embedment of trace impurity of several metal ions within the crystal lattice of natural sphalerite. In addition, the Raman spectra for natural sphalerite exhibited three additional new peaks and shoulders in the spectral region between the transverse-optic (TO) (278 $cm^{-1}$) and LO (347 $cm^{-1}$) modes, which occurred at 298 ($Y_1$), 305 ($Y_2$) and 330 ($Y_3$) $cm^{-1}$ [18,19]. The prominent bands at 298 and 330 $cm^{-1}$ are probably a characteristic feature of tetrahedral Fe–S coordination [19]. The Raman spectra confirmed the foreign metal ions detected in the natural sphalerite sample were in the form of isomorphism, so they partly substitute for $Zn^{2+}$ to form the polynary sulfide without introducing any impurity phases. Due to the presence of substituting metal ions at the $Zn^{2+}$ position with larger ionic radius ($Fe^{2+}$ 0.76 Å; $Cd^{2+}$ 0.97 Å) than $Zn^{2+}$ (0.74 Å), the lattice parameter is reasonably increased, which is consistent with the XRD results.

A typical SEM micrograph of natural sphalerite powder sample was shown in Fig. 3. Cleavage planes and fracture surfaces were prevalent on the surface of the natural sphalerite, which were probably produced by the mechanical grinding. Since cleavage planes and fracture surfaces are known to provide much more active sites than flat crystal faces, the reactivity of natural mineral surface is generally higher than that of its synthetic counterparts with perfect crystal faces.

The zeta-potential profile of natural sphalerite suspension was shown in Fig. 4. The zero point charge was measured at 3.5. For the

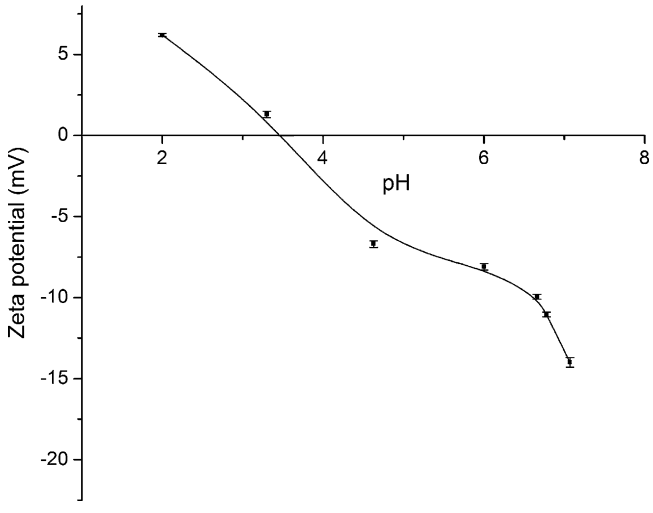


**Fig. 4.** Plots of zeta-potential as a function of pH for natural sphalerite suspension (0.5 g/L), with a starting ionic strength of 0.1 M (NaCl).

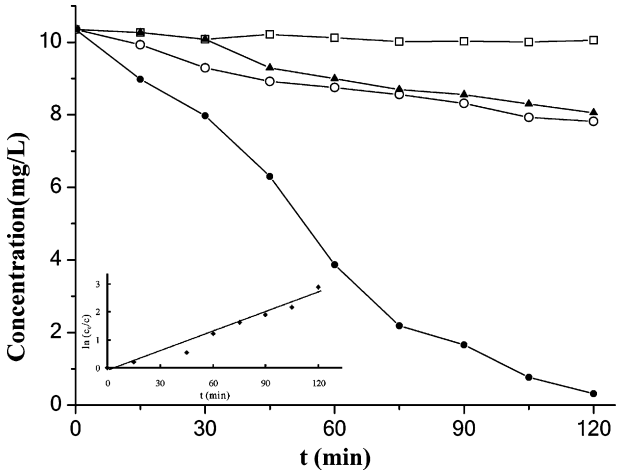


**Fig. 5.** MO degradation in visible light under different controls: (□) MO; (▲) MO + sphalerite; (○) MO + AA; (●) MO + AA + sphalerite. The inset contains the pseudo-first-order reaction kinetics curve for MO photo-reduction by natural sphalerite.

natural sphalerite sample used in this work, the PZC value was much lower than that of the synthetic sphalerite (6.7) [10], which could be attributed to the presences of foreign metal ions and surface defects altering the surface conditions. As a result, the performance of the natural sphalerite sample in photocatalytic reactions was expected to be different from the pure sphalerite.

The BET surface area of natural sphalerite was 1–2 $m^2/g$, much lower than that of the synthesized sphalerite. This is attributed to the difference in particle size, with natural sphalerite in micrometer range and the synthesized sphalerite in nanometer range.

### 3.2. Photocatalytic reduction of MO

#### 3.2.1. Photo-degradability and kinetic analysis

Degradation of MO served as a model reaction system. It was used to investigate the photocatalytic activity of natural sphalerite under visible light irradiation. The changes of MO concentration under different controls in visible light were shown in Fig. 5.

In controls without catalyst and AA, no bleaching was found when under visible light irradiation, indicating that MO was stable under visible light. When AA was added, a slightly bleaching of MO was seen in the absence of catalyst under visible light irradiation. This demonstrated that the photolysis of MO occurred in the presence of ascorbic acid as a sensitizer [20,21]. Although the high energy level of conduction band electrons of sphalerite provides a driving force for MO reduction, the efficiency of MO degradation in the absence of the hole scavenger (AA) was too low after 2 h of irradiation. The results suggest that AA played a key role in the photocatalytic process probably due to its efficient capture of holes.

The complete decolorization of MO by visible light-irradiated natural sphalerite in the presence of hole scavenger (AA) was reached within 2 h, as illustrated in Fig. 5. The plot of the natural logarithm of $c_0/c$ versus time (see Fig. 5, inset) shows approximate linearity, which indicated the photo-degradation fitted a pseudo-first-order kinetic model.

#### 3.2.2. Effect of adsorption

Adsorption of the organic substrate is generally considered to be an important parameter in determining the photo-degradation efficiency [9]. The mode of adsorption also determines the fate of the primary products. The FT-IR spectra of MO and natural sphalerite after MO adsorption are shown in Fig. 6. The intense bands situated at around 1040 and 1168 $cm^{-1}$ were characteristic of the $-SO_2-$ groups symmetric stretching vibration in the sulfonate group of MO

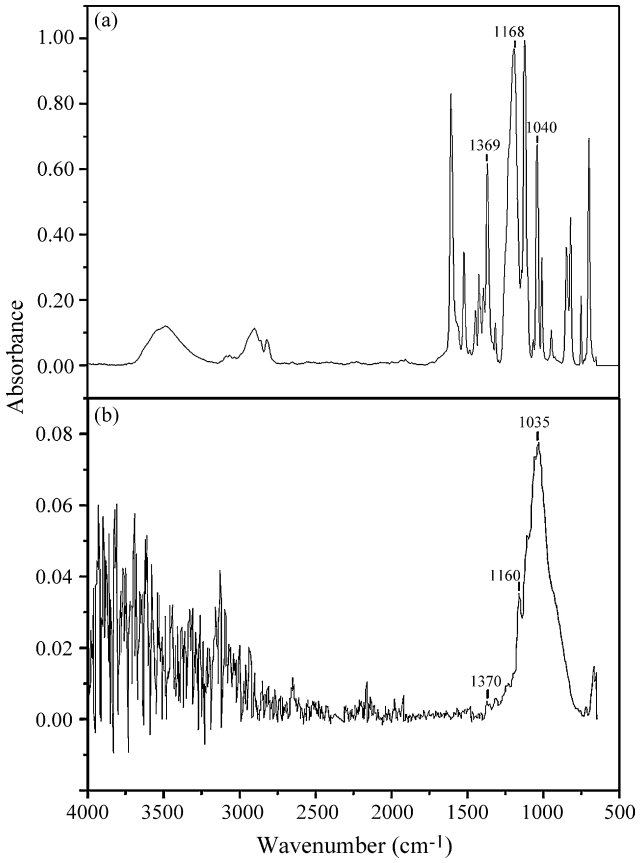


**Fig. 6.** FT-IR spectra of (a) MO and (b) natural sphalerite after MO adsorption.

molecules [22] and the coupling between the benzene mode and $\upsilon_S$ ($SO_3$) [2], respectively. The peak near 1370 $cm^{-1}$ was attributed to the aromatic ring vibration sensitive to the interaction with the azo bond [23]. Compared with the spectra of MO, the coincidence of the peaks at around 1035, 1160 and 1370 $cm^{-1}$ in the spectra of MO adsorbed on spahlerite indicated a successful adsorption of the dye on the catalyst. The ratio of the peak intensities of the bonds at 1160 $cm^{-1}$ to that at 1370 $cm^{-1}$ for the isolated MO is about 6.69. By contrast, this ratio for MO adsorbed on the natural sphalerite decreases to ≈1.59, indicating the group of MO molecule adsorbed on the sphalerite surface was mainly the sulfonate group ($R–SO_3^-$) [2]. This enables the photocatalytic degradation of MO to initiate at the attack of the sulfonate group.

The amounts of MO adsorbed were correlated to the point of zero charge (PZC) of natural sphalerite. When in contact with water, the mineral surface will be hydrated with acidic and alkaline sites [25]. The dissociative interaction of water with the surface of sphalerite releases Zn–OH and S–H groups [25]. When pH values are lower than the PZC of natural sphalerite, the surface could undergo the following equilibrium [9,24]:

$$\equiv ZnOH \qquad \equiv ZnOH_2^+$$
$$+ 2H^+ \rightarrow$$
$$\equiv ZnSH \qquad \equiv ZnSH_2^+ \qquad (1)$$

At the experimental pH of 3.3, $ZnOH_2^+$ and $ZnSH_2^+$ were the predominant surface species, and the sphalerite surface was positively charged. The surface positive charge favored the adsorption of the anionic azo dye MO due to the electrostatic attraction.

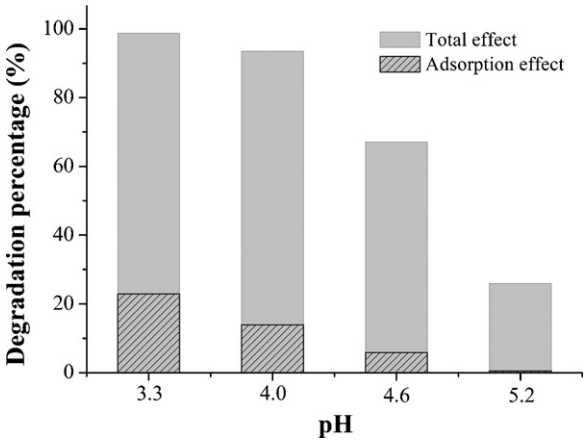


**Fig. 7.** MO degradation by natural sphalerite under different pH values.

### 3.2.3. *Effect of pH*

To determine the influences of the pH on MO degradation, a series of experiments were conducted at different pH values. Since the p$K_a$ of AA is 4.3 [14], the buffering range of the ascorbic–ascorbate mixtures is pH 3.3–5.3. Experiments were conducted under pH 3.3, 4.0, 4.6 and 5.2. It was observed that the degradation efficiency of MO decreased when pH increased (Fig. 7). We hypothesized 3 mechanisms to explain the decrease of the reaction efficiency from pH 3.3 to 5.2.

(1) An increase in $H^+$ concentration favors the reaction:

$$(CH_3)_2NC_6H_4N{=}NC_6H_4SO_3^- + 2H^+ + 2e^- \rightarrow (CH_3)_2NC_6H_4NH{-}NHC_6H_4SO_3^- \quad (2)$$

(2) The adsorption efficiency of MO in 1.5 h was 22.90% (pH 3.3), 13.96% (pH 4.0), 5.86% (pH 4.6) and 0.49% (pH 5.2), respectively, demonstrating that the pH values of the solution might have influenced the electrostatic charge of the catalyst surface. A progressive decrease of positive charge ($ZnOH_2^+$ and $ZnSH_2^+$) on the sphalerite surface would decrease the amount of adsorbed anionic MO, thereby causing lower photocatalytic efficiency. The results also demonstrated that adsorption was the dominant condition for the photocatalysis.

(3) The p$K_a$ of MO is 3.5. When pH is below 3.5, the MO is in its protonated form following the equilibrium [5]:

$$\underset{\text{(azo structure)}}{(CH_3)_2NC_6H_4N{=}NC_6H_4SO_3^-} + H^+ \Leftrightarrow \underset{\text{(quinoid structure)}}{(CH_3)_2N^+C_6H_4N - NHC_6H_4SO_3^-} \quad (3)$$

The quinoid structure of MO is more easily reduced than its azo structure [26].

### 3.3. *Identification of degradative intermediates and final products*

The main intermediates and final products were identified based on the UV–vis absorption spectra, coupled with an accurate analysis of FT-IR and ESI-MS spectra.

UV–vis spectra obtained from the MO solution at experimental pH (pH 3.3) were shown in Fig. 8. The UV–vis absorption of MO was characterized by the maximal band located at 503 nm ($\lambda_{max}$ of the protonated form of MO). As the irradiation progressed, the disappearance of the absorption band at 503 nm indicated the destruction of the –N=N– azo structure in MO molecular.

In comparison with the FT-IR spectra of the sphalerite powder sample before reaction (see Fig. 8, inset), the spectra after the photocatalytic reaction did not show any new bands, indicating the intermediates or products were desorbed from the catalyst surface. In order to investigate the fate of the main intermediates and products, the photoreaction solutions were analyzed by FT-IR.

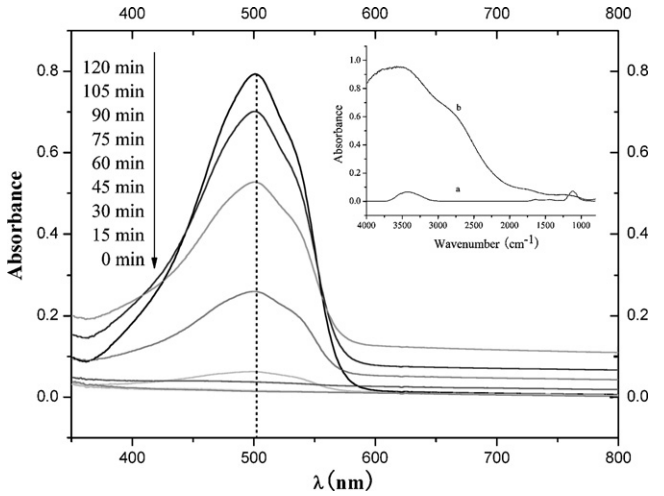


**Fig. 8.** UV–vis absorption spectra of MO at specific time intervals during the visible light photo-reduction of MO. The inset contains the FT-IR spectra of natural sphalerite (a) before and (b) after the photocatalytic reaction.

Fig. 9 gives the FT-IR spectra of the reaction solutions after 2 h of visible light irradiation. The strong absorption band at 1683 $cm^{-1}$ in blank solution was attributed to the quinoid structure of MO, while the solution after the photocatalytic reaction did not show this band, implying a complete destruction of the quinoid structure. The absorption peak at 1117 $cm^{-1}$ corresponds to $SO_4^{2-}$ ions. Both of the solutions from blank and photocatalytic experiments exhibited this peak, which implies that $SO_4^{2-}$ was probably a final product, possibly resulting from the sulfonate group of MO. The release of $SO_4^{2-}$ in the solution from blank experiment could be accounted for by a photo-assisted hydrolysis [2,27]:

$$R{-}SO_3^- + H_2O \rightarrow R{-}H + HSO_4^- \quad (4)$$

$$HSO_4^- \Leftrightarrow SO_4^{2-} + H^+ \quad (5)$$

However, such a reaction might be included in but not account for the photocatalysis of natural sphalerite, because the intensity of $SO_4^{2-}$ peak in the photocatalytic reaction solution was much stronger. The possible way of the generation of $SO_4^{2-}$ ions could be:

$$\text{Spalerite} + h\upsilon \rightarrow e^- + h^+ \quad (6)$$

$$R{-}SO_3^- + e^- + H^+ \rightarrow R^\bullet + HSO_4^- (\rightarrow SO_4^{2-} + H^+) \quad (7)$$

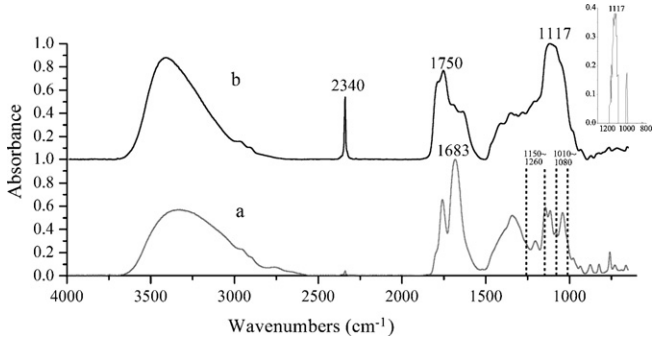


**Fig. 9.** FT-IR spectra of (a) blank and (b) photocatalytic reaction solutions after 2 h visible light irradiation. The inset contains the spectrum for suspensions containing sphalerite exposed to light in the absence of MO subtracted from the spectrum (b).

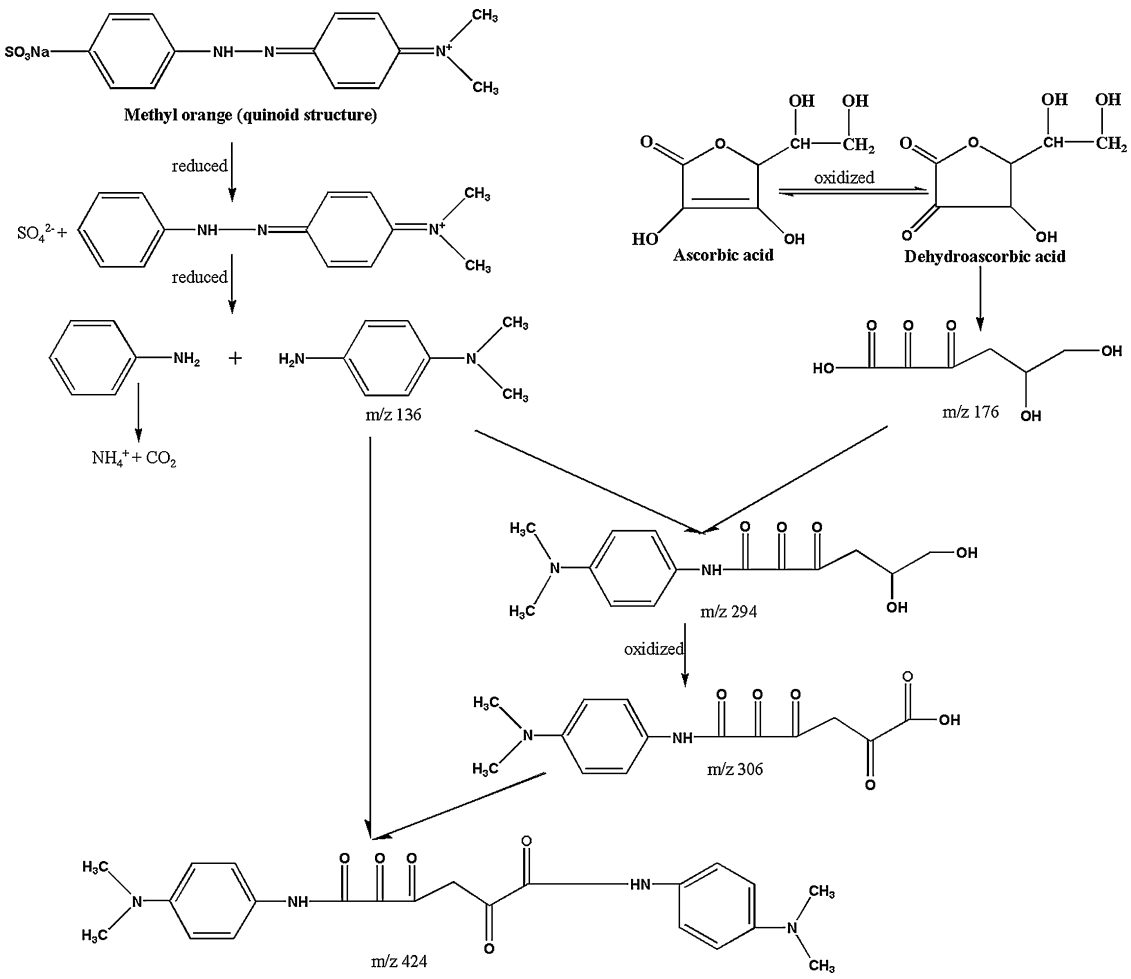


**Scheme 1.** Proposed pathway for linking the possible intermediates formed in MO photo-reductive process.

The attack of sulfonate group would be favored since the dye was adsorbed with its R–$SO_3^-$ onto the mineral surface [2,28]. An alternative explanation for the $SO_4^{2-}$ peak is that it might be in part due to the oxidation of sphalerite. If the spectrum for suspensions containing sphalerite exposed to light in the absence of the azo dye was subtracted from the Fig. 9(b), the $SO_4^{2-}$ peak at 1117 $cm^{-1}$ still existed (see Fig. 9, inset). The result confirmed the generation of $SO_4^{2-}$ from sulfonate group by photocatalysis (reactions (6) and (7)). Then, the radical R• would undergo a further degradation to other intermediates. The bands in the regions of 1010–1080 $cm^{-1}$ and 1150–1260 $cm^{-1}$ were assigned to sulfonate group (R–$SO_3^-$). In the solution from the blank experiment, the dense absorbance in these regions was observed; while in the solution from the photocatalysis experiments, these bands mostly disappeared, indicating that the sulfur-containing species were eliminated due to the destruction of R–$SO_3^-$ containing structures by the photocatalysis.

Formations of the degradative intermediates were further identified by using positive ion mode ESI-MS and may be linked through the pathway shown in Scheme 1. The analytes of interest included protonated $[M+H]^+$, sodiated $[M+Na]^+$ and kaliated $[M+K]^+$. A product holding *m*/*z* 136 was identified as N,N-dimethyl-p-benzenediamine, which was formed from the loss of p-amino benzene sulfonic acid radicals during MO degradation. No radicals of p-amino benzene sulfonic acid were detected. This suggests that the species might be further decomposed into the correspondent derivatives of $SO_4^{2-}$, $CO_2$ and $NH_4^+$. The assumption was consistent with the IR spectrum (Fig. 9(b)), in which the strong bands of $SO_4^{2-}$ (1117 $cm^{-1}$) and $CO_2$ (2340 $cm^{-1}$) were observed in the photoreaction solution. The formation of a species holding $[M+H]^+$ 177 was presumably from the oxidation of AA. The presence of this compound suggests that AA was a strong hole scavenger, and it could rapidly react with photo-generated hole before holes could neutralize electrons. Thus the conduction band electrons could be preserved to react with MO. In additions, AA was sacrificial because it underwent an irreversible oxidation. The intermediates holding *m*/*z* 294 were due to the oxidized derivatives from AA reacting with N,N-dimethyl-p-benzenediamine. It could be further oxidized into another species holding *m*/*z* 306, which went through a further reaction with N,N-dimethyl-p-benzenediamine to form a product holding *m*/*z* 424.

### 3.4. Mechanisms of MO photo-reduction under visible light

#### 3.4.1. Spectra responding performance

Fig. 10 shows the diffuse reflectance UV–vis absorption spectra for natural sphalerite. There are two types of absorption in the visible light region, a steep absorption edge at around 420 nm and a broad shoulder band in the region of 450–600 nm. The steep absorption edge was attributed to the intrinsic interband transition. The weak but significantly broad shoulder band at longer wavelength was assigned to the discrete levels in the bandgap, indicating the presence of impurity levels arising from defects [29]. The bandgap energy ($E_g$) estimated from the onset of the steep absorption edge was 2.95 eV [29]. The response to visible light of natural sphalerite was mainly correlated to the existences of isomorphous substitutions of host metal ions by foreign ions in the crystal lattices.

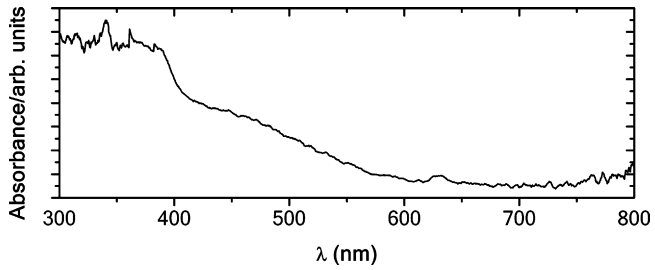


**Fig. 10.** Diffuse reflectance UV–vis absorption spectra of natural sphalerite.

Previous studies indicated that the substitution of $Zn^{2+}$ with $Fe^{2+}$ decreased the band gap [30], and the bandgap of $Zn_{1-x}Cd_xS$ solid solution decreased along with the decreasing of $x$ [31,32]. Hence, the isomorphous substitutions (mainly Fe and Cd) for Zn modified the electronic property of the sphalerite and altered its band structure.

With the strong absorption of visible light assigned by those two absorption types, expectedly natural sphalerite possesses a visible light-induced photoactivity.

### 3.4.2. Conduction band potential

Fig. 11 illustrated the conduction band potential of sphalerite and the reduction potential of MO and $O_2$ as a function of pH. The reduction potential of MO and $O_2$ used in Fig. 11 was obtained from the literature [10]. The conduction band potential of natural sphalerite was calculated by using the empirical formula proposed by Halouani and Deschavres [33] and Sculfort and Gautron [34], i.e.:

$$E_C = (\chi_M^a \chi_X^b)^{1/a+b} - \frac{1}{2}E_g + 0.059(pH_{PZC} - pH) + E_0 \quad (8)$$

where $\chi_M$ and $\chi_X$ are the absolute electronegativity of the atoms M and X for a $M_aX_b$ compound, $E_g$ represents the bandgap, and $E_0$ is the scale factor relating the reference electrode redox level to the AVS ($E_0 = -4.5$ V for NHE) [35]. For the sample used in this work, $\chi_{Zn} = 4.45$ eV, $\chi_S = 6.22$ eV [36], $E_g = 2.95$ eV and $pH_{PZC} = 3.5$. Hence, the EC can be approximately expressed as:

$$E_{C(vs.\ NHE)} = -0.40 - 0.059pH \quad (9)$$

Obviously, the large difference between the conduction band and the reduction potential of MO act as the strong thermodynamic driving force for MO photo-reduction; however, the presence of $O_2$ in the solution may compete with MO in accepting conduction band electrons, therefore reduce the photo-reductive efficiency of dye by natural sphalerite.

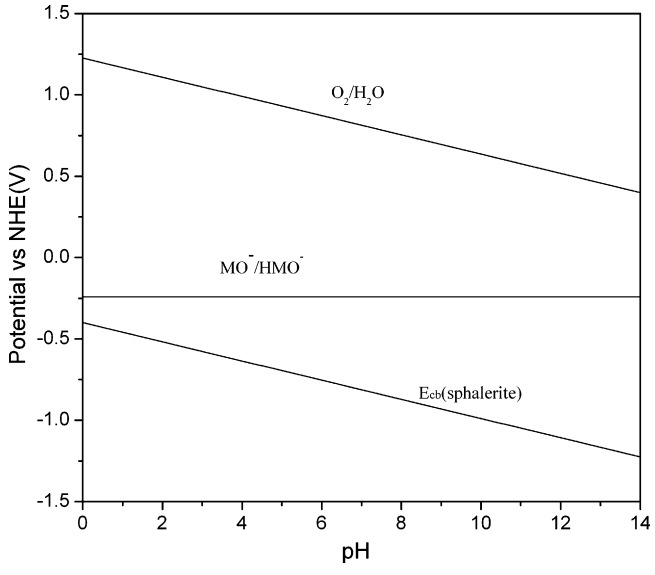


**Fig. 11.** Conduction band energy level of natural sphalerite and the redox potentials of relevant species as a function of pH.

### 3.4.3. Proposed pathway for the photocatalytic reaction

On the basis of our results and the cited literature, we propose that photocatalytic reduction of MO may include: adsorption of MO, surface photocatalytic reaction, and desorption of final products. Upon light irradiation, the valence band electrons are excited to conduction band, facilitating the formation of electron–hole pairs. Ascorbic acid, as a sacrificial hole scavenger, is effectively oxidized and simultaneously supply electrons to valence band holes. The high efficiency of MO photo-reduction might be achieved by AA, which reacts irreversibly with the photo-generated holes, thereby resulting in an efficient charge transfer to suppress the recombination of electron–hole pairs. Then, a direct electron transfer from natural sphalerite to the adsorbed MO gives the negative radical $MO^{\bullet -}$, which can be subsequently converted into $MOH^{\bullet}$ after protonation. This mechanism was proposed based on the observation that the dye was adsorbed onto the catalyst surface, making electron transfer between the dye and the catalyst readily feasible. Subsequently, $MOH^{\bullet}$ undergoes a further reduction, leading to the destruction of –N=N– azo bond and the production of aromatic amines.

## 4. Conclusions

Photocatalytic reaction by natural semiconductor minerals is an emerging technique for decomposing organic contaminants. In this work, we investigated photocatalytic reduction of an azo dye MO by natural sphalerite.

The strong and wide absorption of visible light observed by the diffuse reflectance UV–vis absorption spectra promises the visible light photoactivity of natural sphalerite. The lower redox potential of the conduction band than that of MO provides a driving force for MO photo-reduction. Although there is heterogeneity in the physicochemical properties of natural sphalerite, experimental results from this study suggest that the strong absorptive and good photo-reducing capabilities of natural sphalerite may offer a cost-effective method in treating contaminants such as azo dye MO.

## Acknowledgements

This work was supported by the National Basic Research Program of China (973 Program, Program No. 2007 CB815602) and by the National Science Foundation of China (Grant No. 40572022) awarded to A.H. Lu.

## References

[1] M. Asiltürk, F. Sayılkan, S. Erdemoğlu, M. Akarsu, H. Sayılkan, M. Erdemoğlu, E. Arpaç, Characterization of the hydrothermally synthesized nano-$TiO_2$ crystallite and the photocatalytic degradation of Rhodamine B, J. Hazard. Mater. 129 (2006) 164–170.
[2] M. Karmaz, E. Puzenat, C. Guillard, J.M. Herrmann, Photocatalytic degradation of the alimentary azo dye amaranth mineralization of the azo group to nitrogen, Appl. Catal. B: Environ. 51 (2004) 183–194.
[3] P.B. Dejohn, R.A. Hutchins, Treatment of dye wasters with granular activated carbon, Text. Chem. Color. 8 (1976) 34–38.
[4] Y.M. Slokar, A.M. Le Marechal, Methods of decoloration of textile wastewaters, Dyes Pigments 37 (1998) 335–356.
[5] G.T. Brown, J.R. Darwent, Photoreduction of methyl orange sensitized by colloidal titanium dioxide, J. Chem. Soc., Faraday Trans. 1 80 (1984) 1631–1643.
[6] E.S. Yoo, J. Libra, U. Wiesman, Reduction of azo dyes by desulfovibrio desulfuricans, J. Water Sci. Technol. 41 (2000) 15–22.
[7] S. Kalyushnyi, V. Sklyar, Biomineralisation of azo dyes and their breakdown products in anaerobic–aerobic hybrid and UASB reactors, Water Sci. Technol. 41 (2000) 23–30.
[8] R. Suárez-Parra, I. Hernández-Pérez, M.E. Rincón, S. López-Ayala, M.C. Roldán-Ahumada, Visible light-induced degradation of blue textile azo dye on

$TiO_2$/CdO–ZnO coupled nanoporous films, Sol. Energy Mater. Sol. Cells 76 (2003) 189–199.
[9] C. Hu, Y. Tang, J.C. Yu, P.K. Wong, Photocatalytic degradation of cationic blue X-GRL adsorbed on $TiO_2/SiO_2$ photocatalyst, Appl. Catal. B: Environ. 40 (2003) 131–140.
[10] L. Zang, C.Y. Liu, X.M. Ren, Photochemistry of semiconductor particles 3. Effects of surface charge on reduction rate of methyl orange photosensitized by ZnS sols, J. Photochem. Photobiol. A: Chem. 85 (1995) 239–245.
[11] V. Augugliaro, C. Baiocchi, A.B. Prevot, E. García-López, V. Loddo, S. Malato, G. Marcí, L. Palmisano, M. Pazzi, E. Pramauro, Azo-dyes photocatalytic degradation in aqueous suspension of $TiO_2$ under solar irradiation, Chemosphere 49 (2002) 1223–1230.
[12] Y. Li, A.H. Lu, C.Q. Wang, Photocatalytic reduction of $Cr^{VI}$ by natural sphalerite suspensions under visible light irradiation, Acta Geol. Sin-Engl. 80 (2006) 267–272.
[13] I.M. Arabatzis, T. Stergiopoulos, D. Andreeva, S. Kitova, S.G. Neophytides, P. Falaras, Characterization and photocatalytic activity of $Au/TiO_2$ thin films for azo-dye degradation, J. Catal. 220 (2003) 127–135.
[14] J. Peral, A. Mills, Factors affecting the kinetics of methyl orange reduction photosensitized by colloidal CdS, J. Photochem. Photobiol. A: Chem. 73 (1993) 47–52.
[15] M. Krauzman, Spectre Raman du second ordre de la blende ZnS, C. R. Acad. Sci. Ser. B (1968) 1224–1226.
[16] L. Couture-Mathieu, J.P. Mathieu, Raman spectra of ZnS, Compt. Rend. 236 (1953) 371–385.
[17] G.A. Hope, R. Woods, C.G. Munce, Raman microprobe mineral identification, Miner. Eng. 14 (2001) 1565–1577.
[18] M. Zigone, M. Vandevyver, D.N. Talwar, Raman scattering and local force variations due to transition-element impurities in zinc-sulfide crystals: effect of pressure application, Phys. Rev. B 24 (1981) 5763–5778.
[19] S.J. Sandoval, A.L. Rivera, J.C. Irwin, Influence of reduced mass differences on the Raman spectra of ternary mixed compounds: $Zn_{1-x}Fe_xS$ and $Zn_{1-x}Mn_xS$, Phys. Rev. B 68 (2003) 3031–3039.
[20] G.R. Seely, On the chlorophyllide-sensitized reduction of azobenzene and other compounds, J. Phys. Chem. 69 (1965) 2779–2782.
[21] A.K. Chibisov, Impulse photolysis study of oxidative-reductive reactions photosensitized by pigments, Biofizika 12 (1967) 53–62.
[22] X.S. Feng, M.Y. Yu, H.G. Liu, D.J. Qian, J. Mu, Studies on the composite Langmuir–Blodgett films of tetracationic porphyrazine cobalt and methyl orange, Langmuir 16 (2000) 9385–9389.
[23] C. Bauer, P. Jacques, A. Kalt, Investigation of the interaction between a sulfonated azo dye (AO7) and a $TiO_2$ surface, Chem. Phys. Lett. 307 (1999) 397–406.
[24] R. Gärd, A. Holmgren, W. Forsling, Spectroscopic studies of dextrin adsorption onto colloidal ZnS, J. Colloid Interface Sci. 194 (1997) 319–325.
[25] N. Serpone, P. Maruthamuthu, P. Pichat, E. Pelizzetti, H. Hidaka, Exploiting the interparticle electron transfer process in the photocatalysed oxidation of phenol, 2-chlorophenol and pentachlorophenol: chemical evidence for electron and hole transfer between coupled semiconductors, J. Photochem. Photobiol. A: Chem. 85 (1995) 247–255.
[26] A. Mills, G. Williams, Methyl orange as a probe of the semiconductor–electrolyte interfaces in CdS suspensions, J. Chem. Soc., Faraday Trans. 1 83 (1987) 2647–2661.
[27] A.A. Mackay, J.J. Pignatello, Application of fenton-based reactions for treating dye wastewaters: stability of sulfonated azo dyes in the presence of iron (III), Helv. Chim. Acta 84 (2001) 2589–2600.
[28] A. Lachheb, E. Puzenat, A. Houas, M. Ksibi, E. Elaloui, C. Guillard, J.M. Herrmann, Photocatalytic degradation of various types of dyes (Alizarin S, Crocein Orange G, Methyl Red, Congo Red, Methylene Blue) in water by UV-irradiated titania, Appl. Catal. B: Environ. 39 (2002) 75–90.
[29] A. Kudo, I. Tsuji, H. Kato, $AgInZn_7S_9$ solid solution photocatalyst for $H_2$ evolution from aqueous solutions under visible light irradiation, Chem. Commun. (2002) 1958–1959.
[30] Y. Xu, M.A.A. Schoonen, D.R. Strongin, Thiosulfate oxidation: catalysis of synthetic sphalerite doped with transition metals, Geochim. Cosmochim. Acta 60 (1996) 4701–4710.
[31] N. Kakuta, K.H. Park, M.F. Finlayson, A. Ueno, A.J. Bard, A. Campion, M.A. Fox, S.E. Webber, J.M. White, Photoassisted hydrogen production using visible light and coprecipitated ZnS CdS without a noble metal, J. Phys. Chem. 89 (1985) 732–734.
[32] A.W.H. Mau, C.B. Huang, N. Kakuta, A.J. Bard, A. Campion, M.A. Fox, J.M. White, S.E. Webber, Hydrogen photoproduction by Nafion/cadmium sulfide/platinum films in water/sulfide ion solutions, J. Am. Chem. Soc. 106 (1984) 6537–6542.
[33] F.E. Halouani, A. Deschavres, Interface semi-cinductur-electrolyte: correlations entre le potential de bande plate les echelles d'electronegative, Mater. Res. Bull. 17 (1982) 1045–1052.
[34] J.L. Sculfort, J. Gautron, The role of the anion electronegativity in semiconductor–electrolyte and semiconductor–metal junctions, J. Chem. Phys. 80 (1984) 3767–3773.
[35] J.O.M. Bockris, S.U.M. Khan, Surface Electrochemistry: a Molecular Level Approach, vol. 1014, Plenum, New York, 1993.
[36] R.G. Pearson, Absolute electronegativity and hardness: application to inorganic chemistry, Inorg. Chem. 27 (1988) 734–740.